

# G-virial: Gravity-based structure analysis of molecular clouds<sup>★</sup>

Guang-Xing Li<sup>1</sup>, Friedrich Wyrowski<sup>1</sup>, Karl Menten<sup>1</sup>, Tom Megeath<sup>2</sup>, and Xun Shi<sup>3</sup>

<sup>1</sup> Max-Planck Institut für Radioastronomie, Auf dem Hügel, 69, 53121 Bonn, Germany

<sup>2</sup> University of Toledo, Ritter Astrophysical Observatory, Department of Physics and Astronomy, Toledo OH 43606

<sup>3</sup> Max-Planck-Institut für Astrophysik, Karl-Schwarzschild-Straße 1, 85740 Garching bei München, Germany

June 11, 2021

## ABSTRACT

We present the G-virial method which aims to quantify (1) the importance of gravity in molecular clouds in the position-position-velocity (PPV) space, and (2) properties of the gas condensations in molecular clouds. Different from previous approaches that calculate the virial parameter for different regions, our new method takes gravitational interactions between all the voxels in 3D PPV data cubes into account, and generates maps of the importance of gravity. This map can be combined with the original data cube to derive relations such as the mass-radius relation. Our method is important for several reasons. First, it offers the ability to quantify the centrally condensed structures in the 3D PPV data cubes, and enables us to compare them in an uniform framework. Second, it allows us to understand the importance of gravity at different locations in the data cube, and provides a global picture of gravity in clouds. Third, it offers a robust approach to decomposing the data into different regions which are gravitationally coherent. To demonstrate the application of our method we identified regions from the Perseus and Ophiuchus molecular clouds, and analyzed their properties. We found an increase in the importance of gravity towards the centers of the individual molecular condensations. We also quantified the properties of the regions in terms of mass-radius and mass-velocity relations. Through evaluating the virial parameters based on the G-virial, we found that all our regions are almost gravitationally bound. Cluster-forming regions appear are more centrally condensed.

**Key words.** General: Gravitation – ISM: structure – ISM: kinetics and dynamics – Stars: formation – Methods: data analysis

## 1. Introduction

Star formation takes place in the dense and shielded parts of the interstellar medium. Observations show that the interstellar medium exhibits complicated, irregular, and filamentary structures (Goldsmith et al. 2008; Men'shchikov et al. 2010; Schneider & Elmegreen 1979; Williams et al. 2000). Theoretically, such structures are created by various physical processes such as turbulence, gravity, magnetic field, and radiation.

To understand star formation it is necessary to understand how various physical processes affect it. Gravity is a long-range interaction, and plays important roles in most astrophysical processes at a multiple of physical scales. This is particularly true for turbulent molecular clouds (e.g., Heyer et al. 2009; Kauffmann et al. 2013). However, characterizing the role of gravity on a cloud at various physical scales is not straightforward.

In observations, the structure of molecular gas can be traced by spectral lines in the 3D PPV (position-position-velocity) space where molecular gas exhibits complicated structures. However, given the rich information obtained observationally, few constraints on the role of gravity in the clouds have been obtained so far. One major difficulty is to properly quantify the irregular structure of the gas. The virial parameter  $\alpha_{\text{vir}} = 5\sigma^2 R/GM$ <sup>1</sup> is commonly used to quantify the importance of gravity, and to calculate it we must define a region in which  $\sigma$

and  $M$  can be evaluated.<sup>2</sup> As a result, the virial parameter is only suitable for the cases where the structures are well defined. The morphology of the molecular interstellar medium is generally so complicated that in many cases it is difficult to separate individual objects from a continuous distribution of material. This has been further complicated by the fact that we observe the structures of the sky plane, and the structures identified from the observations are biased by various projection effects (Beaumont et al. 2013; Dib et al. 2006; Pichardo et al. 2000; Shetty et al. 2010).

Another difficulty with the virial parameter is that it is localized. To define the virial parameter we need to define the region, and by evaluating the virial parameter of that region, we automatically neglect the gravitational interaction between the region and its surroundings. As a result, the virial parameter can be used to quantify the importance of gravity for the individual structures, but it cannot be used to understand the importance of gravity for a cloud as a whole. Gravity is a long-range interaction, and to understand its importance, we need to understand how it works not it one region on one particular physical scale, but on a multiple of physical scales.

One case where such an understanding is required is the cluster-forming region. In observations, such regions are found to be centrally condensed in both the position-position space and the PPV space, and physically we expect that gravity is important at the centers of the cluster-forming regions and should become less important if we move from the centers to the out-

Send offprint requests to: Guang-Xing Li, e-mail: gxli@mpi-fr-bonn.mpg.de, gxli@usm.lmu.de

<sup>★</sup> Available at <http://gxli.github.io/G-virial/>.

<sup>1</sup> Here  $\sigma$  is the velocity dispersion and  $M$  is the mass (Bertoldi & McKee 1992). The surface terms and the magnetic terms are neglected. See Ballesteros-Paredes (2006) for a thorough discussion.

<sup>2</sup> Such regions have been defined with the `clumpfind` (Williams et al. 1994) and the `dendrogram` (Rosolowsky et al. 2008) programs in the past.

skirts. This stratification, which is of crucial importance for understanding stellar clustering, awaits to be quantified.

In this paper we introduce a new method called *G-virial* (available at <https://gxli.github.com/G-virial>) to quantify the importance of gravity in a variety of situations where mass is traced in the 3D PPV space. Instead of dividing the molecular cloud into regions based on iso-intensity contours in the 3D data cube (e.g., Williams et al. 1994), the method takes the gravitational interactions between all the voxels in the 3D PPV data cube into account, and generates maps of the importance of gravity in 3D. As a result, it provides constraints on the global importance of gravity. This is complementary to methods that calculate the self-gravity such as the virial parameter. Such a map of the importance of gravity also enables us to identify gravitationally coherent regions in molecular clouds and to quantify the structures of the regions.

In this paper, we introduce the *G-virial* method (section 2 – 5), and explore its usage in quantifying the importance of gravity and the structures of the molecular condensations seen in simulations (section 5) and observations (section 6). We conclude in section 7.

## 2. Problem formulation

Observationally, molecular gas can be mapped by rotational transitions of molecules such as CO. Through proper modeling of the emission, it is possible to construct the distribution of the molecular gas in the form of a 3D PPV data cube which covers a continuous  $(x, y, v)$  space

$$m(x, y, v) = \tilde{\rho}(x, y, v) dx dy dv, \quad (1)$$

where  $m$  represents the mass,  $x$  and  $y$  represent the spatial dimensions, and  $v$  represents the velocity dimension. Here  $\tilde{\rho}$  has a dimension of  $M L^{-3} T$ , and represents the amount of mass per unit area per unit velocity. The distribution of  $\tilde{\rho}$  in the  $v$  dimension represents the distribution of gas at different velocities along the same line of sight.

We start with a mass distribution in a 3D PPV data cube (Fig. 1). We aim to understand how a particle at voxel  $i$  is bound by mass from all the voxels  $j$  (not excluding  $i$ ). To achieve this, we split our task into two subtasks. First, we need to estimate the gravitational boundedness of voxel  $i$  by another voxel  $j$  in the 3D PPV data cube. Second, we need to estimate the gravitational boundedness of a voxel  $i$  based on the information we have about all the other voxels  $j$ .

### 2.1. Boundedness of a voxel pair in a 3D data cube

We start by defining the gravitational boundedness between a pair of voxels  $(i, j)$ . We are interested in the extent to which a particle  $i$  is bound to another voxel  $j$ . For our purpose,  $i$  can be treated as a massless test particle, and the boundedness of particle  $i$  is determined by the mass of the voxel  $j$ .

The available measurable quantities in 3D PPV data cube include the mass  $m_j$ , the spatial separation  $\delta r_{ij}$  and the velocity separation  $\delta v_{ij}$ . We expect the boundedness to increase with  $m_j$  and decrease with  $\delta r_{ij}$  since gravitational attraction increases with the mass and decreases with the distance.

The remaining question is how to make use of the information contained in the velocity direction. We expect that voxels with large velocity differences are not likely to be bound to each other, for two reasons. First, a larger velocity separation implies higher kinetic energy, which consequently decreases the

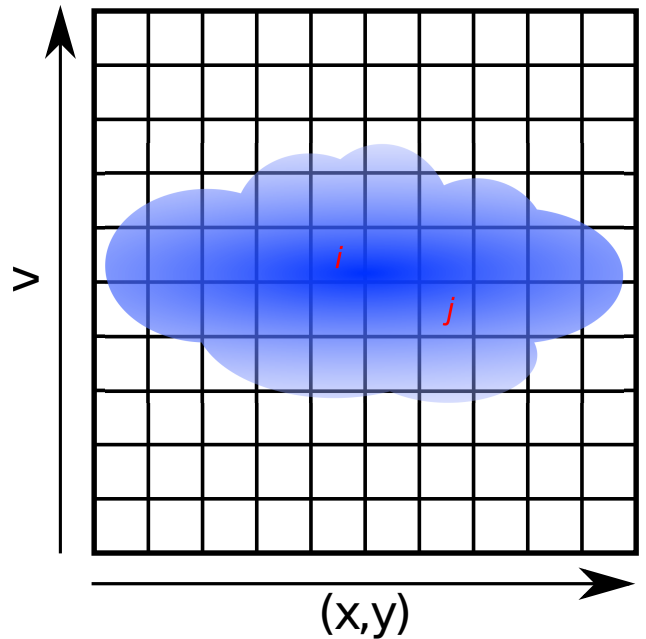


Fig. 1: Setup of the problem. We consider a mass distribution in a 3D PPV data cube. This is represented as the black grid.  $x$ - $y$  represents the spatial dimensions and  $v$  represents the velocity dimension. The mass distribution is represented in blue. For each voxel  $i$ , its *G-virial* can be determined by taking its interactions with all the voxels  $j$  (not excluding  $i$ ) into account. See Sect. 2 for details.

likelihood of it being gravitationally bound. Second, it has been found that the molecular gas follows the Larson's relation (Larson 1981)<sup>3</sup> where the spatial length and velocity dispersion are related by

$$\delta v \sim \delta r^{1/2}. \quad (2)$$

As a result, a larger velocity separation implies a larger spatial separation, which implies a lower gravitationally boundedness.

Here, we define the gravitational boundedness contributed from voxel  $j$  to voxel  $i$  as

$$I_{j \rightarrow i} = \frac{G m_j}{\delta r_{ij} \delta v_{ij}^2}. \quad (3)$$

The boundedness  $I_{j \rightarrow i}$  increases with mass and decreases with spatial and velocity separation.

Apparent similarities exist between Eq. 3 and the virial parameter. The virial parameter is defined as (Bertoldi & McKee 1992)<sup>4</sup>

$$\alpha_{\text{vir}} = \frac{G m}{5 \sigma_v^2 r}, \quad (4)$$

where  $m$ ,  $r$ , and  $\sigma_v$  are the mass, radius, and velocity dispersion of the clumps. The virial parameter is a measurement of the gravitational boundedness of an object. The quantity  $I_{j \rightarrow i}$  defined by Eq. 3 has a dimension of  $G \text{ Mass} / \text{Radius}$

<sup>3</sup> In Larson (1981) the index is 0.38. In Roman-Duval et al. (2011) the index is found to be 0.51.

<sup>4</sup> Here our virial parameter is  $E_p/2 E_k$ , and in Bertoldi & McKee (1992) the virial parameter is  $2 E_k/E_p$ .

Velocity<sup>2</sup>, which is the same as that of the virial parameter. Therefore, Eq. 3 can be viewed as a generalization of the virial parameter to a voxel pair, and a larger  $I_{j \rightarrow i}$  is related to a larger chance for voxel  $i$  to be bounded by voxel  $j$ .

## 2.2. The G-virial

We define the G-virial of a voxel  $i$  as the sum of the gravitational boundedness contributed from all the voxels  $j$  (not excluding  $i$ ). To be more precise,

$$\begin{aligned} \alpha_{\text{G-virial}}^i &\equiv \sum_j I_{j \rightarrow i} \\ &= G \times \sum_j \frac{m_j ((x_i - x_j)^2 + (y_i - y_j)^2)^{-\frac{1}{2}}}{(v_i - v_j)^2} \\ &= G \times \sum_j \frac{m_j}{((x_i - x_j)^2 + (y_i - y_j)^2)^{\frac{1}{2}} (v_i - v_j)^2}, \end{aligned} \quad (5)$$

where  $I_{j \rightarrow i}$  comes from Eq. 3, and in the second step we take into account that the G-virial is measured in the 3D PPV space. The physical meaning of Eq. 5 can be understood as follows. For one voxel  $i$ , its G-virial is determined by summing up its boundedness with all the other voxels  $j$ .

In Eq. 5, if  $j$  is close to  $i$  in both the spatial and the velocity direction, it contributes more to the G-virial. The contribution is proportional to the mass  $m_j$ , and inversely proportional to  $\delta r_{ij}$  and  $\delta v_{ij}^2$ .

For a continuous distribution of material, Eq. 5 can be written as

$$\alpha_{\text{G-virial}}(x, y, v) = \int \frac{G \tilde{\rho}(x', y', v')}{((x - x')^2 + (y - y')^2)^{1/2} (v - v')^2} dx' dy' dv', \quad (6)$$

where the integration is carried out over the whole data cube. Here  $\tilde{\rho}$  has a dimension of  $M L^{-2} V^{-1}$  where  $M$  is mass,  $L$  is size, and  $V$  is velocity.

If the separation between  $i$  and  $j$  becomes small, the denominator of Eq. 6 approaches zero and the integrand can become large. If the density distribution is smooth, the term

$$\frac{\tilde{\rho}(x, y, v)}{((x_i - x_j)^2 + (y_i - y_j)^2)^{1/2}},$$

is still finite and does not induce a singularity. However, the term

$$\frac{1}{(v - v')^2}$$

is singular. In our calculations, we change it to

$$\frac{1}{(v - v')^2 + c_0^2}, \quad (7)$$

which means we suppress the contribution to the G-virial when the velocity separation is smaller than  $c_0$ , and in our case,  $c_0$  is comparable to the sound speed. We introduce this cutoff in order to make the integrand convergent. Nevertheless, there is a physical reason behind this. In a molecular cloud, the velocity dispersion that we observe comes from two parts: one from the thermal motion, and the other from the large-scale streaming motion of the gas. The first part is almost scale-independent, and the second part increases with the physical size. We are

mainly interested in the balance between gravity and the large-scale streaming motion, and as a result, it is reasonable to discard the contributions where  $\delta v \lesssim c_0$ . In our calculations,  $c_0$  is chosen to be  $1 \text{ km s}^{-1}$ , which is comparable to the sound speed. The effect of changing  $c_0$  influences the absolute values of the G-virial; however, the relative values of the G-virial stay unchanged (Appendix B). Therefore, the G-virial is a relative measure of the gravitational boundedness. In the case where the G-virial map of several observations needs to be compared, a single value of  $c_0$  needs to be chosen in advance.

The reasons for the name G-virial in Eq. 5 include the following: first, we named it G-virial to emphasize its connection with the commonly used *virial parameter*; second, we added the letter G to emphasize that our virial parameter is a generalized version of the virial parameter and that it is *global*. Different from the case of Bertoldi & McKee (1992) and Goodman et al. (2009) where the virial parameter is used to quantify self-gravity, our G-virial takes all the gravitational interactions between gas in the data cube into account. More clarifications concerning the concept of the G-virial can be found in Appendix A.

## 3. Separating components with different velocities

One difficulty that we need to deal with is the line-of-sight confusion. When calculating the G-virial, different components along the same line of sight are distinguished through their velocities. If two components happen to have the same velocity, the G-virial will be over-estimated, since physically unassociated components will be treated as one single component in the calculations.

We argue that in many cases, the separation in the velocity axis provides information so that we can separate different components based on the velocity difference or at least alleviate the problem. We consider two cases; the first is the line-of-sight confusion in a given molecular cloud, and the second is the line-of-sight confusion in our Milky Way disk.

In a molecular cloud, the line-of-sight confusion problem can be alleviated if the molecular gas follows the Larson's relation (Larson 1981; Roman-Duval et al. 2011) because the boundedness is proportional to  $I \sim \delta_r^{-1} \delta_v^{-2}$  (Eq. 3) where  $\delta_r$  and  $\delta_v$  are the separations in position and velocity direction, respectively. We consider two points along the same line of sight separated by  $\delta_z$ . According to the Larson's relation, the velocity dispersion (which is a width of the statistical distribution velocity separation between the two points) is  $\delta_v \sim \delta_z^{1/2}$ . Therefore, the boundedness related to  $\delta_z$  by  $I \sim \delta_v^{-2} \sim \delta_z^{-1}$ . In other words, the contribution is not likely to be large since the velocity is likely to be different in an averaged sense.

In the case of the Milky Way disk, different spiral arms usually have different velocities, they will be separated easily in our calculations. We note that in Eq. 3 the interaction is proportional to  $\delta r^{-1}$  and  $\delta v^{-2}$ . Therefore, a small separation in velocity will lead to a much bigger decrease in interaction and finally make the contribution to the total G-virial negligible. Since the method uses velocity difference to deal with line-of-sight confusion, it is more accurate for the cases where the velocity increases with distance (e.g., including systematic expansion and contraction where velocity increases with distance).

## 4. Numerical procedure

In the case of a 3D PPV data cube, for a voxel  $(x, y, v)$ , the **G-virial** is defined as (see Eqs. 6 and 7)

$$\alpha_{\text{G-virial}}(x, y, v) = \int \frac{G \tilde{\rho}(x', y', v')}{((x-x')^2 + (y-y')^2)^{1/2} (v-v')^2 + c_0^2} dx' dy' dv', \quad (8)$$

where the integration is carried out over the whole data cube. With an observationally constructed distribution of mass in the 3D PPV data cube, we can easily construct the **G-virial** using Eq. 8.

Equation 8 takes the form of a convolution, and can be conveniently calculated in Fourier space. In real space, the kernel is

$$K_x = \frac{1}{(x^2 + y^2)^{1/2} (v^2 + c_0^2)}, \quad (9)$$

and in Fourier space it can be shown that<sup>5</sup>

$$K_k = \frac{2\pi}{(k_x^2 + k_y^2)^{1/2}} \frac{\pi e^{-c_0|k_v|}}{c_0}. \quad (10)$$

Equation 10 enables us to calculate the **G-virial** map efficiently. In our calculations, we first make a 3D Fast Fourier Transform (FFT) to the observationally constructed mass distribution  $\tilde{\rho}(x, y, v)$  and obtain  $\tilde{\rho}_k(k_x, k_y, k_v)$ . Then we calculate the **G-virial** in the Fourier space

$$\alpha_k(k_x, k_y, k_v) = \tilde{\rho}_k(k_x, k_y, k_v) \frac{1}{(k_x^2 + k_y^2)^{1/2}} \frac{\pi e^{-c_0|k_v|}}{c_0}. \quad (11)$$

In the last step the **G-virial** map is obtained by a inverse FFT of  $\alpha_k$ .

We found that the absolute values of the **G-virial** are dependent on  $c_0$  (see Appendix B); however, the relative values of the **G-virial** are insensitive to  $c_0$ . As a result, the **G-virial** is a relative measurement of gravitational boundedness rather than an absolute one. In order for the **G-virial** maps from different regions to be comparable, a unique value of  $c_0$  has to be chosen;  $c_0$  also needs to be larger than the velocity resolution of the observations.

## 5. Quantifying the structure of molecular gas with **G-virial**

We present applications of the **G-virial** to quantify gravity and the structure of molecular gas. To begin with, we apply the method to the models where both the 3D density and 3D velocity structure are available. We focus on two aspects: first, we present the use of **G-virial** in quantifying the importance of gravity in the 3D PPV data cube; second, we quantify the structures of molecular condensations bases on the **G-virial**.

### 5.1. Defining **G-virial** in the PPP space

To properly evaluate the accuracy of the **G-virial** method, we first define the **G-virial**<sup>model</sup> in the PPP space where all the position and velocity information are available, and then compare it with the observationally reconstructed values of the **G-virial**

<sup>5</sup> Here we follow the non-unitary convention.

in the PPV space. Following Equations 3 and 5, we define the model **G-virial** as

$$\alpha_{\text{G-virial}, i}^{\text{model}} = \sum_j I_{j \rightarrow i} = \sum_j \frac{G m_j}{\delta r_{ij} \delta v_{ij}^2}, \quad (12)$$

where

$$\delta r_{ij} = ((x_i - x_j)^2 + (y_i - y_j)^2 + (z_i - z_j)^2 + \delta_x^2)^{1/2}, \quad (13)$$

and

$$\delta v_{ij}^2 = (v_x^i - v_x^j)^2 + (v_y^i - v_y^j)^2 + (v_z^i - v_z^j)^2 + c_{\text{model}}^2. \quad (14)$$

Here the voxel pair  $(i, j)$  has positions  $((x_i, y_i, z_i), (x_j, y_j, z_j))$  and velocities  $((v_x^i, v_y^i, v_z^i), (v_x^j, v_y^j, v_z^j))$ . The parameter  $\delta_x$  is the spatial resolution of the simulation. Writing Eq. 12 in its integral form, we have

$$\alpha_{\text{G-virial}, i}^{\text{model}} = \int \frac{G \rho(x', y', z')}{((x-x')^2 + (y-y')^2 + (z-z')^2 + \delta_x^2)^{1/2}} \times \frac{1}{(v_x(p) - v_x(p'))^2 + (v_y(p) - v_y(p'))^2 + (v_z(p) - v_z(p'))^2 + c_{\text{model}}^2)} \times dx' dy' dz', \quad (15)$$

where  $p$  stand for  $(x, y, z)$  and  $p'$  stand for  $(x', y', z')$ . Here we choose  $c_{\text{model}} = 3 \times c_0$  since the denominator of Eq. 15 is composed of a sum of the velocity difference from the three dimensions. Since the **G-virial** is a relative measure of the gravitational boundedness (Appendix B), our results are not affected by this.

### 5.2. Quantifying the importance of gravity

We study how the importance of gravity traced in the **G-virial** inferred from the simulated observations is related to the **G-virial** theoretically defined in the models.

We consider two models. The first (hydrodynamic simulation model) was taken from a numerical simulation of turbulent gas. The simulation used here was carried out under periodic boundary conditions, and turbulence is injected through compressive forcing mode (Federrath et al. 2008), and no self-gravity is included. The details of the simulations are described in Federrath et al. (2010); Roman-Duval et al. (2011)<sup>6</sup>. Since self-gravity is not included in the simulation, the line-of-sight confusion effect is probably over-estimated because, as was found in Beaumont et al. (2013), in the simulations without gravity structures will overlap more in the PPV space. In this work, we make use of the density and velocity cubes from the simulations.

We make a cutout of a size of  $4.8 \text{ pc} \times 4.8 \text{ pc} \times 4.8 \text{ pc}$  from the snapshot at  $t = 5 T$  where  $T$  is the crossing timescale of the simulation. The computation of Eq. 15 is computationally expensive ( $\mathcal{O}(N^2)$ ). To save computational time, we choose a portion of the simulation with a relatively large gas condensation and relatively complicated internal structures (Fig. 2).

The second model (the analytical model) is constructed to resemble a typical molecular condensation (e.g., McKee & Tan 2003). It is defined within  $r_{\text{in}} < r < r_{\text{out}}$  where  $r$  is the radius,  $r_{\text{in}} = 1 \text{ pc}$ , and  $r_{\text{out}} = 10 \text{ pc}$ . The density structure is

$$\rho(r) = \left(\frac{r}{r_0}\right)^{\gamma_p} \times \rho_0, \quad (16)$$

<sup>6</sup> The simulations are available at <http://starformat.obspm.fr/starformat/documentation.jsp>.

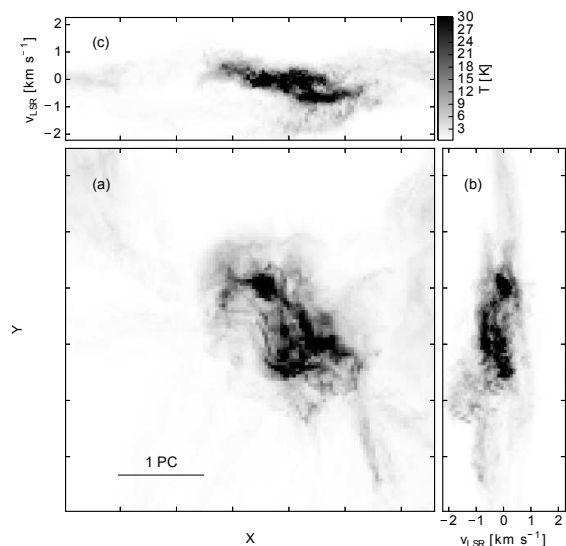


Fig. 2: (a) Map of the peak brightness temperature of the simulated  $^{13}\text{CO}(1-0)$  emission along the velocity axis. (b) Position-velocity map of peak brightness temperatures of  $^{13}\text{CO}(1-0)$  along the Y-axis (c) Position-velocity map of peak brightness temperatures of  $^{13}\text{CO}(1-0)$  along the X-axis.

where  $r_0 = 1$  pc;  $\rho_0 = 10^3 \times m_{\text{H}_2}$ , where  $m_{\text{H}_2}$  is the mass of the  $\text{H}_2$  molecule; and  $\gamma_\rho$  are chosen to vary from  $-1.8$  to  $-2.2$ . The velocity structure is parametrized as

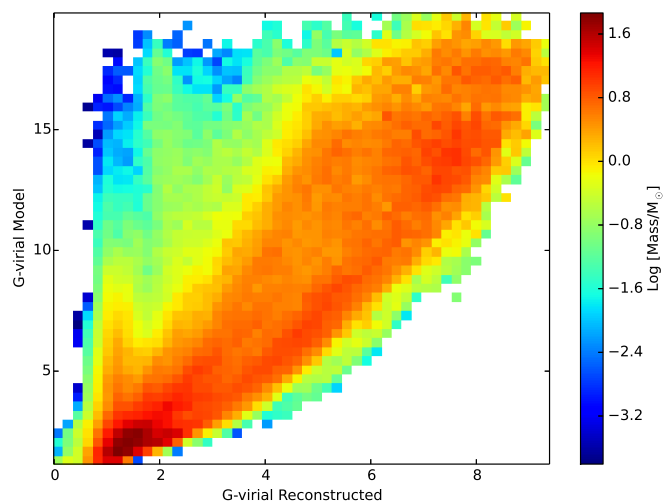
$$v(r) = \left(\frac{r}{r_0}\right)^{\gamma_v} \times v_0, \quad (17)$$

where  $r_0 = 1$  pc,  $\gamma_v$  is chosen to vary from 0.35 to 0.6, and  $v_0 = 1$  km s<sup>-1</sup>. It can be viewed as an expanding sphere. At a given radius, the magnitude of velocity is distributed uniformly between  $0.9 v(r)$  and  $1.1 v(r)$ , and the direction of the velocity is distributed uniformly in 3D. The model is sampled through a total of  $3 \times 10^5$  particles, and then turned into a 3D PPV data cube.

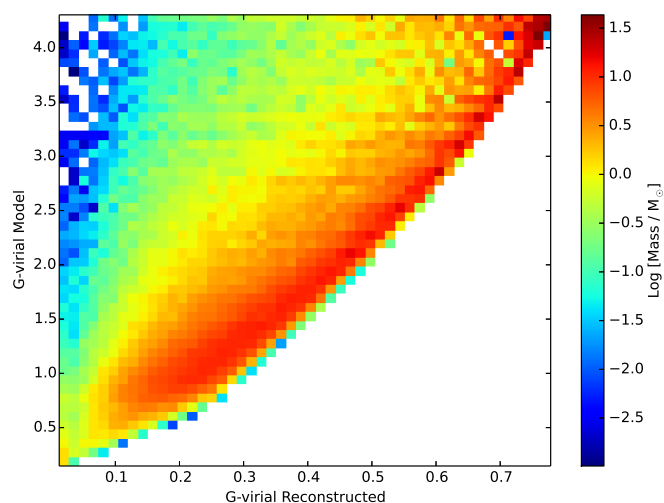
We chose the two models because they represent two typical situations. In the first case (the hydrodynamic simulation model), the model exhibits a high degree of physical complexity. In the second case (the analytical model), the density distribution is centrally condensed, and the model has well-defined mass-radius and velocity-radius structures. We will study the behavior of the G-virial in both cases.

The models are turned into a 3D PPV data cube using a simple radiative transfer model (Sect. 3.3 of Roman-Duval et al. 2011). It is assumed that the  $^{13}\text{CO}(1-0)$  emission is optically thin and  $n(^{13}\text{CO})/n(\text{H}_2) = 1.7 \times 10^{-6}$  (Blake et al. 1987; Langer & Penzias 1990). The excitation temperature is assumed to be 10K. In reality, the  $^{13}\text{CO}(1-0)$  emission can be optically thick and both the abundance and excitation conditions can vary, and these can lead to inaccuracies. However, in testing our method, we are interested in the cases where mass can be reliably traced in the PPV data cube, and observationally this can be achieved by modeling several transitions of CO or using more reliable tracers.

In our calculation of the model G-virial ( $\alpha_{\text{G-virial}}^{\text{model}}$ ), we choose  $c_{\text{model}} = 1$  km s<sup>-1</sup>, and in our calculation of the G-virial reconstructed from the simulated map ( $\alpha_{\text{G-virial}}^{\text{reconstructed}}$ ),



(a) Hydrodynamic simulation.



(b) Analytic model.

Fig. 3: A comparison between the  $\text{G-virial}_{\text{model}}$  calculated from the model and the  $\text{G-virial}_{\text{reconstructed}}$ , which is reconstructed from the simulated observations in the PPV space. (a) shows the result for the hydrodynamic simulation and (b) shows the result for the analytical model with  $\gamma_\rho = -2.2$  and  $\gamma_v = 0.5$ . The colors stand for the amount of mass in a given interval.

we choose  $c_0 = 0.3$  km s<sup>-1</sup>. We make this choice because in Eq. 15 all three velocity components are considered, and in Eq. 6 only one velocity component is considered. Since G-virial is a relative measure of the gravitational boundedness (Appendix B), the conclusions are not dependent on this.

In Fig. 3 we compare the  $\text{G-virial}_{\text{model}}$  calculated from the model with the  $\text{G-virial}_{\text{reconstructed}}$  reconstructed from the simulated observations in the PPV space. The first thing to be noticed is that the absolute values of the G-virial differ because the G-virial is only a relative measure of the gravitational boundedness, rather than an absolute one.

In general, a larger  $\text{G-virial}_{\text{model}}$  is related to a larger  $\text{G-virial}_{\text{reconstructed}}$ . The reconstructed G-virial exhibits a higher uncertainty in the hydrodynamic simulation model since its flow has complicated structures.



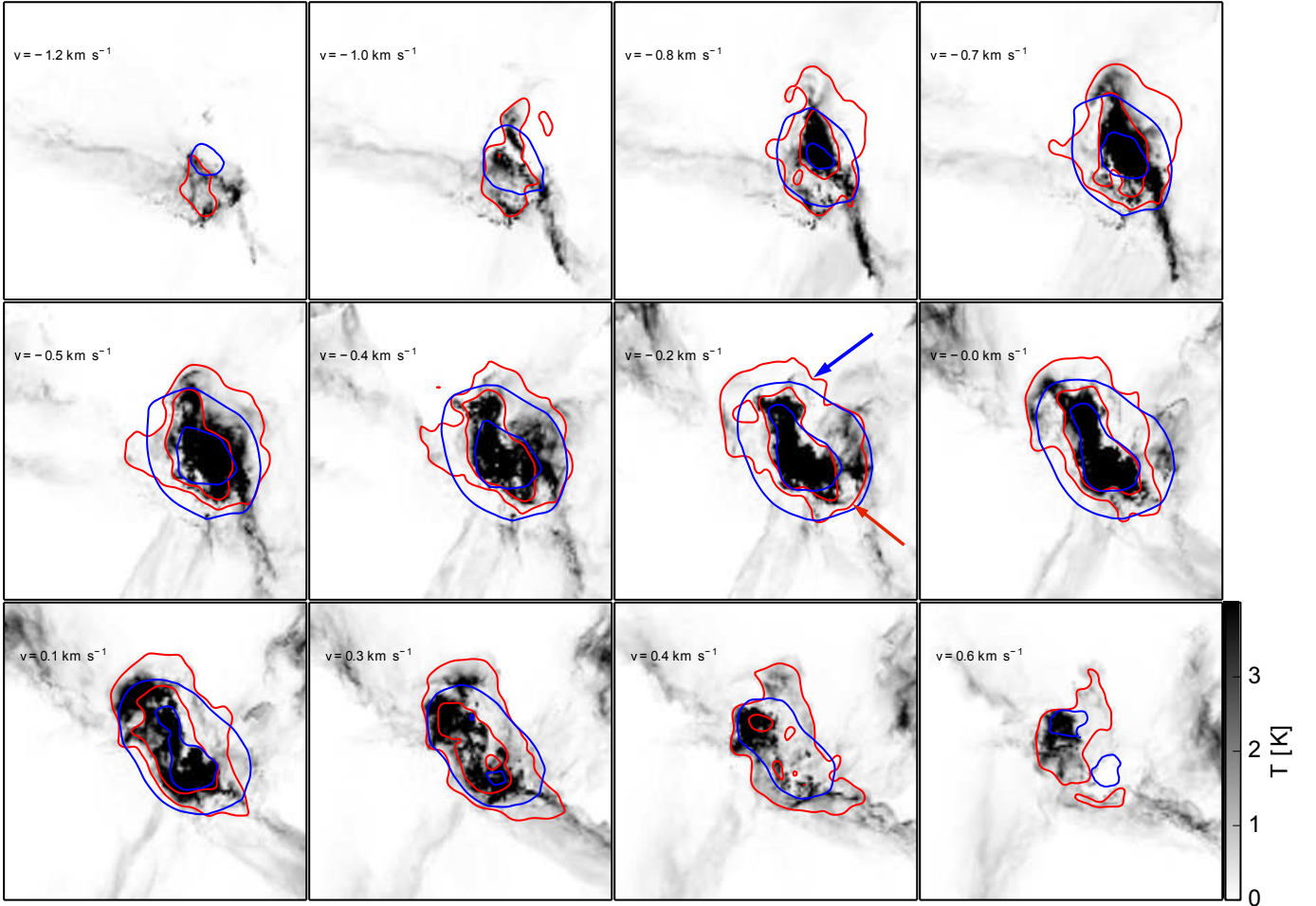


Fig. 4: A comparison between  $G\text{-virial}_{\text{model}}$  and  $G\text{-virial}_{\text{reconstructed}}$  in the PPV space for the hydrodynamical model described in Sect. 5.2. In the model, turbulence is injected through compressible forcing, and no self-gravity is included (Federrath et al. 2008). The  $G\text{-virial}_{\text{model}}$  in the PPV space is defined as the mass-weighted average of the  $G\text{-virial}_{\text{model}}$  in the PPP space, which is defined in 12. Here, the grayscale image is the simulated  $^{13}\text{CO}(1-0)$  emission from the model. The red contours stand for the  $G\text{-virial}_{\text{model}}$ , and the contour levels are (6, 5, 10). The blue contours stand for the  $G\text{-virial}_{\text{reconstructed}}$ , and the contour levels are (3, 6). It worth noting that the  $G\text{-virial}_{\text{model}}$  and the  $G\text{-virial}_{\text{reconstructed}}$  agrees better at regions where mass is traced. This can be seen in the  $v = -0.2 \text{ km s}^{-1}$  channel. They agree better at the regions where mass is traced (e.g., the red arrow), but does not agree well at the region without mass (e.g., the blue arrow).

To look further into the relation between  $G\text{-virial}_{\text{model}}$  and  $G\text{-virial}_{\text{reconstructed}}$ , we convert the  $G\text{-virial}_{\text{model}}$  from the PPP space into the PPV space, and study the connection between the two (Fig. 4). At a given velocity interval, the  $G\text{-virial}_{\text{model}}$  in the PPV space is defined as the mass-weighted average of the  $G\text{-virial}_{\text{model}}$  in the PPP space, and the average is carried over the entire line of sight. There are some significant differences between the iso-  $G\text{-virial}_{\text{model}}$  contours (isosurfaces where the  $G\text{-virial}$  takes constant values) and iso-  $G\text{-virial}_{\text{reconstructed}}$  contours: the iso-  $G\text{-virial}_{\text{model}}$  exhibit more structures and iso-  $G\text{-virial}_{\text{reconstructed}}$  is smoother because the  $G\text{-virial}_{\text{model}}$  is unaffected by the line-of-sight confusion. Thus, the  $G\text{-virial}$  map constructed in the PPV space is better suited to studying the effect of gravity at large scale, but is not suitable for the study of the importance of gravity at small scale (e.g., individual cores). Although the iso-  $G\text{-virial}_{\text{model}}$  and the iso-  $G\text{-virial}_{\text{reconstructed}}$  does not agree completely, they agree better at positions where emission is enhanced and mass is traced,

and tends to differ more where there is little emission. Since we are interested in the gravitational boundedness of the gas, this disagreement at regions where little mass is present is not as important as it might appear.

Since the hydrodynamic simulation model exhibit complicated structures, the line-of-sight confusion has a larger impact on the results than the case of the analytical model. However, in the gravity-free hydrodynamic simulation model the confusion probably has been over-estimated. According to Beaumont et al. (2013), structures tend to overlap more without self-gravity.

### 5.3. Quantifying the internal structures

For a given region, its  $G\text{-virial}$  map is centrally concentrated, and if we divide the region based on different isosurfaces of  $G\text{-virial}$  values, we get a set of regions that nest inside one another. We propose to quantify the structures of the gas condensations in the PPV space with the mass-radius relation and

velocity dispersion-radius relation derived with the help of the isosurfaces of the G-virial.

Inside a closed region where the G-virial of the voxels is larger than a given threshold, we can evaluate parameters such as mass, radius, and velocity dispersion. Using a map of mass distribution  $m(x, y, v)$  and a map of the G-virial  $\alpha_{G\text{-virial}}(x, y, v)$ , the corresponding parameters are evaluated by taking all the voxels inside a given contour of the  $\alpha_{G\text{-virial}}(x, y, v)$  map into account. The mass of a region is defined as

$$m = \int_R \bar{\rho}(x, y, v) dx dy dv, \quad (18)$$

where  $R$  denotes a coherent region that satisfies  $\alpha_{G\text{-virial}}(x, y, v) > \alpha_{\min}$  and the central velocity of a region is defined as

$$v_0 = \frac{\int_R \rho(x, y, v) v dx dy dv}{\int_R \rho(x, y, v) dx dy dv}. \quad (19)$$

The velocity dispersion is defined as

$$\sigma_v = \left( \frac{\int_R \rho(x, y, v) (v - v_0)^2 dx dy dv}{\int_R \rho(x, y, v) dx dy dv} \right)^{1/2}. \quad (20)$$

The radius of the region is defined by diagonalizing the tensor of second moments of the position coordinates weighted by the intensity (Goodman et al. 2009), and is defined as

$$R = 1.91 \times (\sigma_{\min} \sigma_{\max})^{1/2}, \quad (21)$$

where  $\sigma_{\min}$  and  $\sigma_{\max}$  are the dispersions along the major and minor axes.

This set of definitions enables us to quantify the structure of molecular condensations observed in the PPV space in terms of mass-radius and velocity dispersion-radius relations. If the molecular gas has a relatively diffuse morphology, we expect to see a steeper dependence of the enclosed mass  $M$  with the radius  $r$ ; if the molecular gas is centrally condensed, we expect to see a shallower  $M$ - $r$  dependence. Similar arguments can be applied to the dependence of velocity dispersion on radius  $\sigma_v$ - $r$ .

If the molecular gas is centrally condensed, the  $M$ - $r$  and  $\sigma_v$ - $r$  relations of the gas condensations are well defined in the PPP (position-position-position) space. It is expected that we can reconstruct these relations observationally with the help of the G-virial. If a molecular gas condensation has a diffuse and irregular morphology, these G-virial-derived relations can still represent the morphology of the gas condensations. The difference between different regions can be represented in the  $M$ - $r$  and  $\sigma_v$ - $r$  planes.

To demonstrate the diagnostic power of the  $M$ - $r$  and  $\sigma_v$ - $r$  relations, we generated a set of models with different density and velocity structures, and compare them with the  $M$ - $r$  and  $\sigma_v$ - $r$  relations reconstructed with the G-virial (Fig. 5). The differences in structure among different regions can be accurately reconstructed with the help of the G-virial. Furthermore, the slope of the  $M$ - $r$  and  $\sigma_v$ - $r$  relations are accurately reconstructed with the G-virial<sup>7</sup>.

<sup>7</sup> To make the G-virial-derived relations overlap with the model values, we scaled the estimated radius by a factor of 1.4 and the estimated velocity dispersion by a factor of 1.45. This adjustment is made in order to make it easier to compare different curves. In practice, the radii of the estimated regions are based on the tensor of second moments of the position coordinates, and the radii do not necessarily coincide with the radii defined in the model. A similar argument also applies to the estimation of the velocity dispersion.

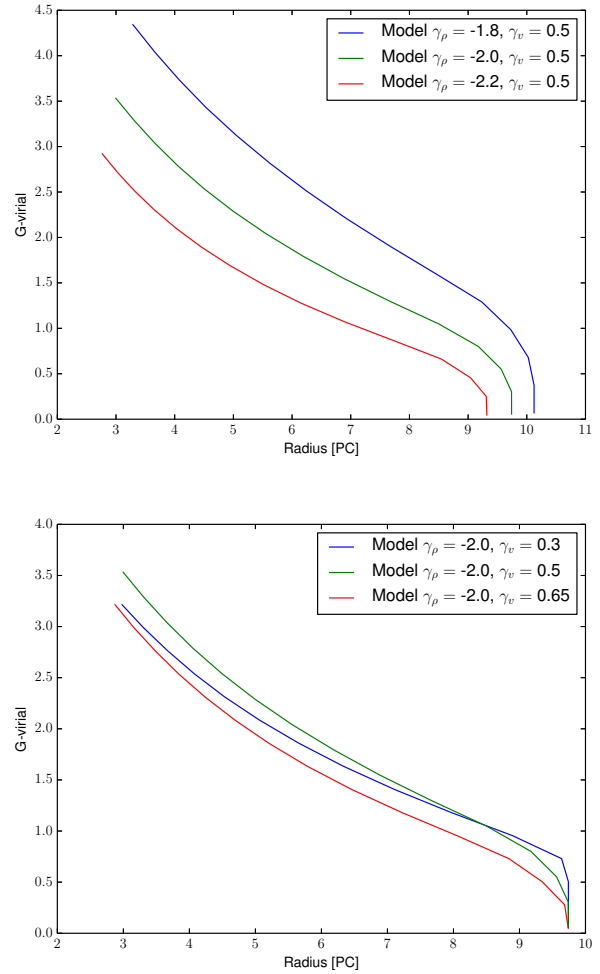


Fig. 6: G-virial as a function of radii for models with different  $\gamma_\rho$  and  $\gamma_v$ .

We also plot the dependence of G-virial as a function of radius for various models (Fig. 6). For all the models, we found an increase of G-virial towards the centers of the regions. Larger G-virial are found for the models with more condensed structure and lower velocity dispersion.

#### 5.4. Short summary

In this section we demonstrated the usage of G-virial to quantify the structure of molecular gas condensations. We summarize our findings and remind the reader of the caveats.

We found that the G-virial can be used to quantify the importance of gravity and to quantify the structures of the gas condensations.

1. The G-virial measured from the PPV data cube is positively related to the G-virial found in the model (PPP space), and a larger G-virial is related to a larger probability of being gravitationally bound by the ambient gas.
2. The G-virial map can be used to derive mass-radius and velocity dispersion-radius relations. The G-virial-derived relations are good reconstructions of the structures of the models when the models are symmetric, and can also provide good representations of the structures if the models are irregular.

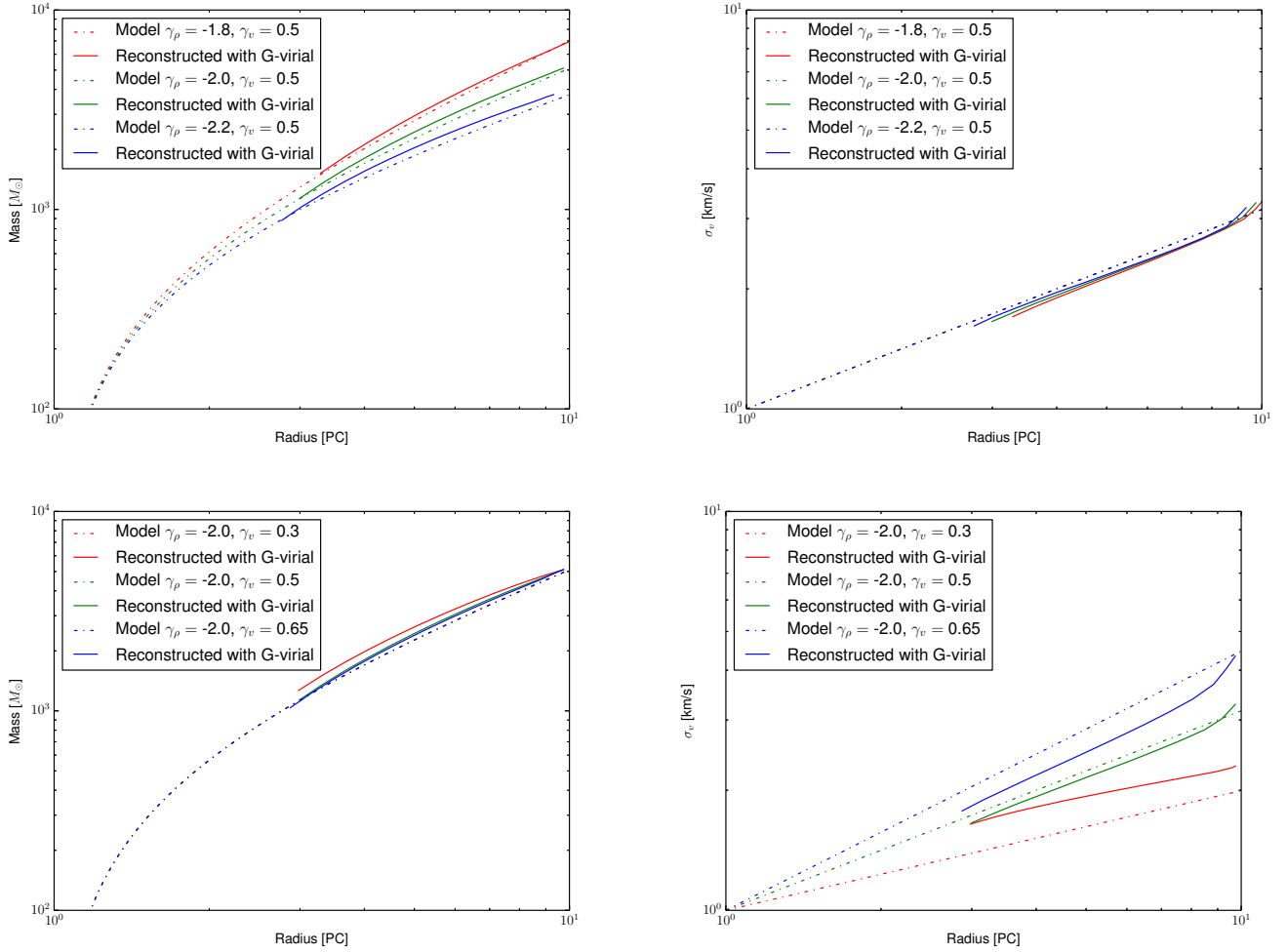


Fig. 5: Comparison between the structure of the model and the structure reconstructed through the G-virial for different sets of model parameters. The upper panels show the results where the analytical model is constructed with different  $\gamma_\rho$ , and the lower panels show the results where the analytical model is constructed with different  $\gamma_v$ . The left panels are the mass-radius relations and the right panels are the velocity dispersion-radius relations. Here the radius is scaled up by a factor of 1.4 and the velocity dispersion is scaled up by a factor of 1.45 for an easy comparison.

Several caveats need to be noted. First, the G-virial is a relative measure of the gravitational boundedness. A larger G-virial means a larger change of being gravitationally bound. The absolute values of the G-virial cannot be directly used to tell if a region is gravitationally bound or not. The absolute values of the G-virial are dependent on  $c_0$ . Therefore, in order for the values of G-virial from several maps to be comparable, a unique value of  $c_0$  needs to be chosen in advance. This value should be comparable to the sound speed of the medium, and in this work we have chosen it to be  $c_0 = 1 \text{ km s}^{-1}$ . We also note that the G-virial is reconstructed from the PPV space where the projection effect tends to smear out structures; it is more suitable for the study of the gravitational boundedness of the structures larger than the individual gas condensations.

Second, the G-virial method can be used to derive the mass-radius and velocity dispersion-radius relations for molecular condensations. However, the results need to be properly interpreted. If the structures of the gas condensations are regular and are close to being spherically symmetric, the G-virial-derived mass-radius and velocity dispersion-radius relations should be good reconstructions of the real 3D structure. If the structure of

the gas condensations are irregular, the G-virial can be used to derive these relations. However, in this case, the G-virial-derived relations should be viewed as representations of the compactness of the structures in the PPV space, and are not necessarily related to the compactness of the structures in the PPP space.

Finally, we would like to emphasize that the G-virial method works in the PPV space, and like other methods, its accuracy is limited by line-of-sight contamination. The method relies on using the velocity difference to alleviate the line-of-sight confusion. This requires different gas components to have different velocities, which is satisfied in many cases. For a single object, this requires the velocity separation to increase with radius. Whereas this generally holds for individual molecular clouds and clumps, it does not hold for some cores or disks where the velocity decreases with radius (e.g., collapsing cores).

## 6. Applications to molecular clouds

In this section we present applications of our method to several molecular clouds. Our method requires a map of the distribution of molecular gas in the 3D PPV space. Observationally, this can



be conveniently achieved using rotational transitions of the CO molecule.

In the simplest case, this can be achieved by observing the  $^{13}\text{CO}(1-0)$  transition alone. Assuming an excitation temperature of 10 K, a  $^{12}\text{CO}$  abundance of  $X(^{12}\text{CO}/\text{H}_2)=8\times 10^{-5}$ , and a  $^{12}\text{CO}$  to  $^{13}\text{CO}$  ratio of  $R(^{12}\text{CO}/^{13}\text{CO})=45$ , the column density can be estimated as (Roman-Duval et al. 2010; Simon et al. 2001)

$$N(\text{H}_2) = 4.92 \times 10^{20} \times \frac{T_{\text{mb}}}{\text{K}} \times \frac{\delta_v}{\text{km s}^{-1}}, \quad (22)$$

where  $T_{\text{mb}}$  is measured in K and  $\delta_v$  is the velocity resolution of the data cube measured in  $\text{km s}^{-1}$ . Changing the excitation temperature to 20 or 30 K decreases the derived mass by 40% and 92%, respectively (Simon et al. 2001). For an observed  $^{13}\text{CO}(1-0)$  data cube  $T_{\text{mb}}(x, y, v)$ , the mass distribution  $m(x, y, v)$  can be obtained as

$$\frac{m(x, y, v)}{g} = 4.92 \times 10^{20} \times \frac{T_{\text{mb}}(x, y, v)}{\text{K}} \frac{\delta_v}{\text{km s}^{-1}} \times \frac{m_{\text{H}_2}}{g} \times \left(\frac{\delta_x}{\text{cm}}\right)^2, \quad (23)$$

where  $\delta_x$  is the voxel size of the spatial dimension in cm and  $\delta_v$  is the channel width in  $\text{km s}^{-1}$ . The values of  $m$  and  $\bar{\rho}$  in Eq. 6 are related by  $m = \bar{\rho} dx dy dv$ .

We apply our G-virial method to the publicly available data from the COMPLETE survey (Ridge et al. 2006). The observations have a spatial resolution of  $46''$  and a velocity resolution of  $0.067 \text{ km s}^{-1}$ , the mean RMS per channel is  $\sim 0.33 \text{ K}$  in terms of  $T_{\text{A}}^*$ , and the beam efficiency is  $\sim 0.5$ .

With a distance of  $250\pm 50 \text{ pc}$  and a total mass of  $10^4 M_{\odot}$  (Enoch et al. 2006), the Perseus molecular cloud is among the best-studied molecular clouds in the Milky Way. It is composed of several distinct regions: B1, B3, NGC1333, and IC348. The Ophiuchus molecular cloud has a distance of  $125 \text{ pc}$  and a mass of  $7 \times 10^3 M_{\odot}$  (de Geus et al. 1989) and contains clouds L1688 and L1689. In particular, L1688 and NGC1333 are cluster-bearing regions. IC348 also hosts a star cluster; however, it is generally considered older than the other regions in Perseus (Gutermuth et al. 2009).

In this section, we provide a study of the structure of the Perseus and Ophiuchus molecular clouds with our G-virial method. We present maps of the G-virial, together with an analysis of the structure of the regions in the clouds based on the G-virial method.

### 6.1. Maps of the G-virial

In Fig. 7 we channel maps of the G-virial in the 3D PPV space. Three-dimensional renderings of the maps are presented in Appendix C. For both clouds, the  $^{13}\text{CO}(1-0)$  maps contain complicated and filamentary structure, whereas the G-virial maps are smooth and contain fewer structures. Interestingly, higher values of G-virial are reached only at cluster-bearing regions such as NGC1333, IC348, and L1688, and this highlights the importance of gravity in such regions. Different regions are indicated in Fig. 8.

### 6.2. Identification of regions

The G-virial offers a new way to divide the molecular cloud into regions. Previously, this has been done either by visual inspection, or with contour-based algorithms such as clumpfind

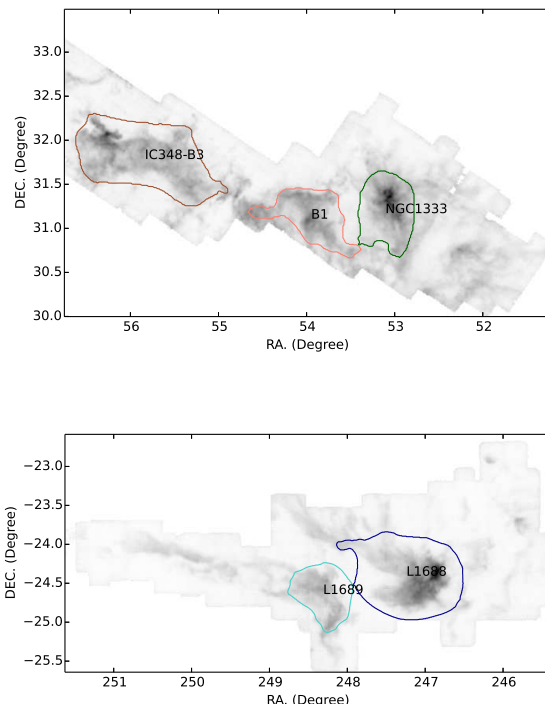


Fig. 8: Regions identified by applying the dendrogram algorithm to our G-virial map. The results from the Perseus molecular cloud (upper panel) and Ophiuchus molecular cloud (lower panel) are presented. The grayscale images correspond to the velocity-integrated  $^{13}\text{CO}(1-0)$  emission and the contours correspond to the projected boundaries of the identified regions. These regions correspond to the “leaves” of the dendrogram. The conventional names of the regions are labeled.

(Williams et al. 1994). It is worth mentioning that other region-finding algorithms are available, such as dendrogram (Rosolowsky et al. 2008) and dochamp (Whiting 2012).

Many of the algorithms (e.g., clumpfind and dendrogram) are contour-based, and they tend to assign voxels to regions based on iso-column-density contours in the 2D case or on iso-intensity contours in the case of a 3D PPV data cube. Molecular clouds are characterized by a set of complicated hierarchical structures, and a naive application of the clumpfind tends to produce hundreds of clumps for one single molecular cloud. It has also been pointed out recently that contour-based methods suffer from superposition and confusion when the volume filling factor of emitting material is large (Beaumont et al. 2013).

In our analysis we are interested in finding gravitationally coherent regions. This can be achieved by applying the dendrogram to the G-virial map, which is a measurement of the gravitational boundedness. Figure 8 shows the regions identified by applying the dendrogram algorithm to our G-virial map. The identified regions correspond to the “leaves” of the dendrogram. In the dendrogram calculations, the minimum difference between different contours is set to 0.4, and the regions correspond to the leaves of the dendrogram. Each identified region consists of a continuous list of voxels in the 3D PPV space. In Fig. 8 the projected boundaries of the regions are plotted<sup>8</sup>.

<sup>8</sup> All the regions were originally defined in 3D.

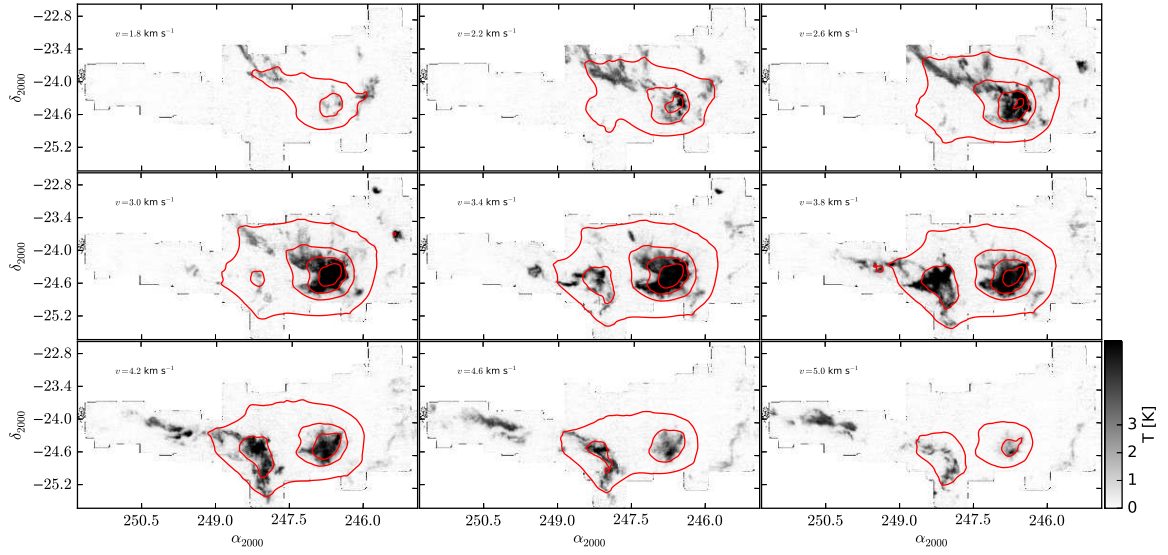
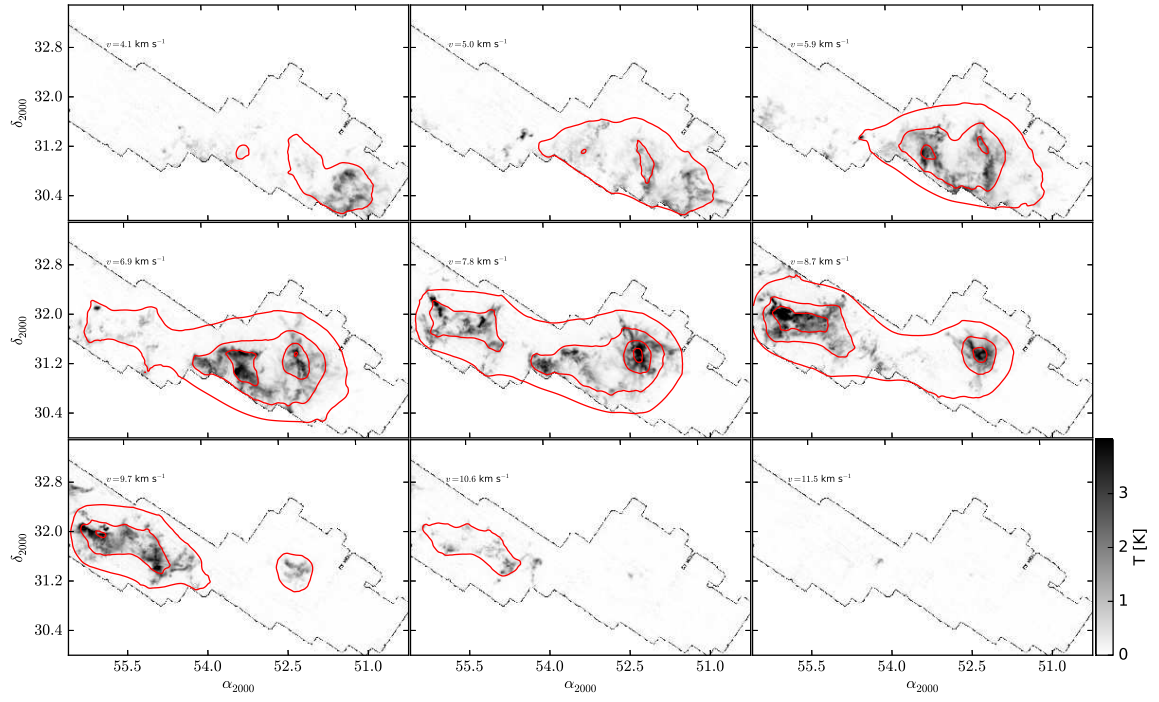


Fig. 7: Channel maps of the  $^{13}\text{CO}(1-0)$  emission and the corresponding G-virial. The upper panel shows the results from the Perseus molecular cloud and the lower panel shows the results from the Ophiuchus molecular cloud. Grayscale images stand for  $^{13}\text{CO}(1-0)$  emission and the red contours represents the G-virial. Contour levels start from 1.2 in steps of 0.8.

Compared to `clumpfind`, a combination of the `G-virial` method and the Dendrogram method tends to identify regions that are coherent while the `clumpfind` tends to break up those regions. The reason is that our `G-virial` maps are much smoother than the original map<sup>9</sup>. Since the `G-virial` maps are much smoother, the results obtained with the `G-virial` maps are much less sensitive to the technical parameters (e.g., the minimum separation of the contours) used in the computations compared to the case with the intensity maps. Therefore, the `G-virial` offers a more robust definition of regions. With `G-virial` we can study the structure of molecular gas in terms of these gravitationally coherent regions. In the 2D case, our method is similar to the `gridcore` code which is based on 2D projected gravitational potential (Gong & Ostriker 2011).

### 6.3. Internal structure of the regions

In this section we study the internal structure of the molecular gas in the individual regions. Previously, the structure of molecular gas was studied in terms of the clumps, and quantified using parameters that are evaluated for the whole clumps. While these methods do provide constraints on the role of gravity inside the regions, the role of gravity on scales larger than the individual gas condensations is neglected. The spatial structure of molecular gas larger than the clump scale can be quantified using the dendrogram algorithm. However, the dendrogram method is contour-based, and only the connection between the adjacent regions in the tree diagram are preserved. This makes it difficult to use dendrogram to quantify the structure of molecular gas on the large scale.

Here we provide an analysis of the structure of the individual regions with the `G-virial` method. As we have shown in section 5.3, the intrinsic mass-radius and velocity-radius relations in the model can be reconstructed with our `G-virial` method to a good accuracy if the velocity dispersion increases with the size.

In Fig. 9 we plot the dependence of velocity  $v_0$  and velocity dispersion  $\sigma_v$  on the radii of the regions. The inner parts of the regions are clearly at the center of the outer part of the regions in velocity space. This means the central part of the regions remains quiescent with respect to the outer parts, and this is consistent with the findings by André et al. (2007); Kirk et al. (2010); Walsh et al. (2004).

We assess the importance of gravity in these regions with the `G-virial` method. In our method, a larger `G-virial` is related to a larger importance of gravity, and as a result the importance of gravity at a given region can be quantified by measuring the amount of gas at different thresholds of the `G-virial` parameter. In Fig. 10, we plot the dependence of gas mass on the `G-virial` threshold for different regions, and in Fig. 11 we plot the dependence of the `G-virial` on the radius. For all the regions, the `G-virial` increases towards the centers. For cluster-bearing regions such as NGC1333 in Perseus and L1688 in Ophiuchus, much higher `G-virial` values have been reached at their centers. This implies that gravity is more important for the clustered mode of star formation.

With our method it is straightforward to derive relations such as the mass-radius and velocity-size relation. Recently, there has been growing interest in quantifying cloud structure in terms of various mass-size relations (e.g., Kauffmann et al. 2010a,b).

<sup>9</sup> This is similar to the case of Smith et al. (2009) where they identified structures from a simulation in the 3D position-position-position space based on gravitational potential.

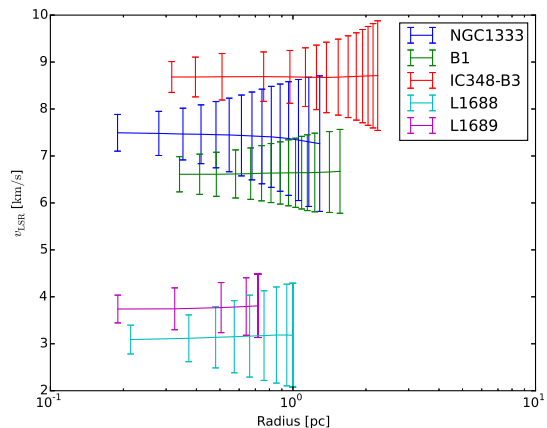


Fig. 9: Dependence of velocity and velocity dispersion as a function of radius. Here the solid lines represent the velocities of the regions, and the bars represent the velocity dispersions of the regions at given radii. The vertical extent of the errorbars are the 3D velocity dispersion  $\sigma_v^{3D} = \sqrt{3} \sigma_v$ .

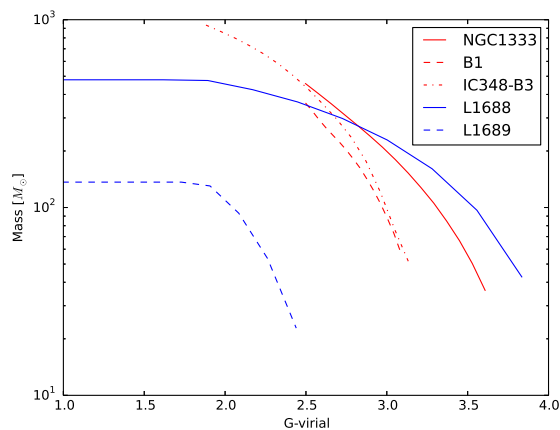


Fig. 10: The amount of molecular gas enclosed in regions with different thresholds of the `G-virial`. The  $x$ -axis is the threshold of `G-virial` which we take to define the region, and the  $y$ -axis is the amount of gas that is enclosed in the region.

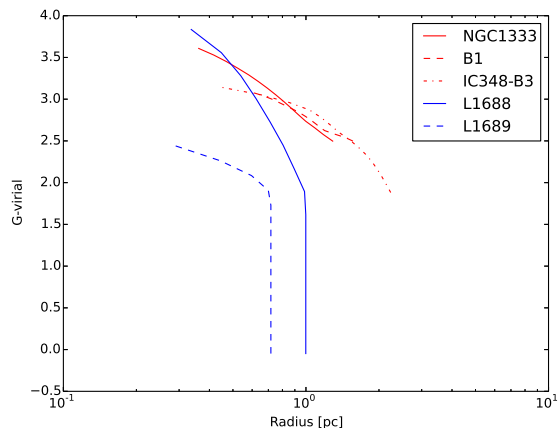


Fig. 11: `G-virial` as a function of radius for different regions.

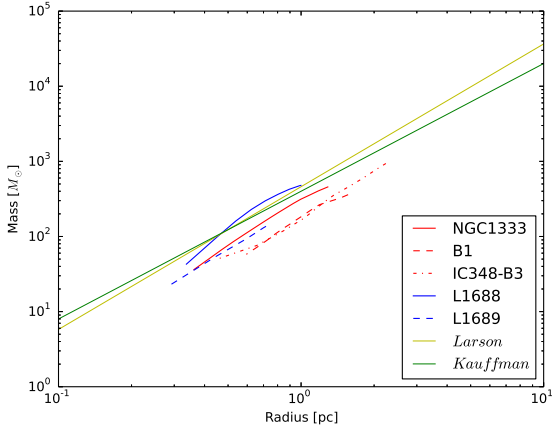


Fig. 12: Enclosed mass as a function of radius for different regions. The scaling relation from Larson (1981) and Kauffmann et al. (2010b) are added. For all the curves, the G-virial decreases with increasing radii.

In Fig. 12 we plot the mass-size relation obtained using our G-virial method (see Section 5). Our mass-size relation is different from that of Kauffmann et al. (2010b) since we use the G-virial contours to define our regions, and mass is evaluated within a given region where the G-virial is larger than the threshold. In Kauffmann et al. (2010b) the mass is evaluated within a region where the column density is larger than a given threshold. In our case, along one single line of sight, only the gas that stays within a given surface of a constant value of the G-virial is taken into account while in Kauffmann et al. (2010b) all the mass along the line of sight is taken into account. Similar to Kauffmann et al. (2010b), we also found that cluster-bearing regions such as L1688 and NGC1333 are more massive in terms of molecular gas than the regions devoid of clusters at a give radius. In Fig. 12 we also plot the scaling relations proposed in Larson (1981,  $m(r) = 460M_{\odot}(r/\text{pc})^{1.9}$ ), and Kauffmann et al. (2010b,  $m(r) = 400M_{\odot}(r/\text{pc})^{1.7}$ ), and found that both provide approximate descriptions of the structure of the regions.

Molecular clouds are believed to be turbulence-dominated, and this is mainly inferred from the fact that the clouds obey the velocity-linewidth relation (Larson 1981). In Fig. 13 we plot the 3D velocity dispersion of our regions as a function of radius. Here the 3D velocity dispersion is  $\sqrt{3}$  times the velocity dispersion evaluated in Eq. 20. The scaling relation from Larson (1981) is also plotted ( $L/\text{pc} \sim 1.01 \times (\sigma_v/\text{km s}^{-1})^{0.38}$ ). In our case, the velocity-linewidth relation is evaluated for centrally condensed objects, and a smaller physical scale is related to the inner part of a gas condensation, whereas in Larson (1981) a smaller physical scale is related to a smaller size of a subregion in a cloud<sup>10</sup>. For our centrally condensed objects, the scaling relation from Larson (1981) seems to be valid. We also note that cluster-bearing regions such as NGC1333 and L1688 have much larger velocity dispersions at large radii.

Heyer et al. (2009) found a dependence of the scaling coefficient  $\sigma_v/r^{1/2}$  of Larson's relation on the column density, and attributed this to the fact that the clouds are in self-gravitational equilibrium. We plot  $\sigma_v/r^{1/2}$  as a function of column density  $\Sigma \equiv M/\pi r^2$ , where  $M$  is the mass and  $r$  is the radius of our

<sup>10</sup> The physical scale here can have different meanings; see Heyer & Brunt (e.g., 2004); Lazarian & Pogosyan (e.g., 2004); Roman-Duval et al. (e.g., 2011).

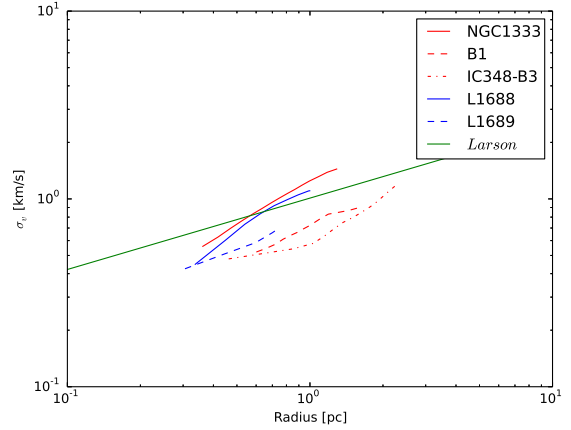


Fig. 13: 3D velocity dispersion as a function of radius for different regions. The velocity-linewidth relation from Larson (1981) is also plotted.

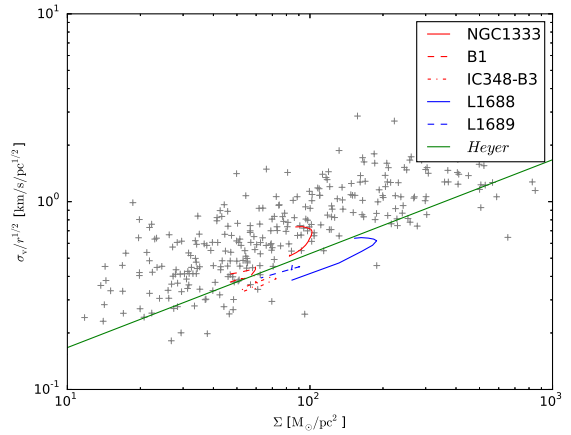


Fig. 14:  $\sigma_v/r^{1/2}$  as a function of column density  $\sigma$  for the regions. In order to be consistent with Heyer et al. (2009),  $\sigma_v$  is the 1D velocity dispersion as defined in Eq. 20 and  $\Sigma \equiv M/\pi r^2$  where  $M$  is the mass  $r$  is the radius. The solid straight line shows the boundary below which the structures are gravitationally bound. It is defined as  $\sigma_v/r^{1/2} = (\pi G/5)^{1/2}\Sigma^{1/2}$ . The gray crosses come from the catalogue of giant molecular clouds studied in Roman-Duval et al. (2010).

regions (Fig. 14). Since we decompose one region into a set of nested subregions based on the G-virial, one single region will appear as a curve in Fig. 14. All our regions are quite close to being gravitationally bound, and the scatter around the y-axis is much smaller than what is found for Milky Way molecular clouds as studied in Heyer et al. (2009). This difference arises mainly from the fact that the G-virial method tends to identify regions that are gravitationally coherent.

## 7. Conclusion

### 7.1. Results and perspectives

In this paper we proposed a general method (G-virial) for studying the structure molecular clouds. Different from the previous methods which decompose molecular clouds based on



contours in the 2D plane or 3D PPV data cubes, in this method a map is generated by taking all the gravitational interactions between all the voxels in the 3D data cubes into account.

The generated 3D G-virial maps have a dimensionless unit that is the same as that of the virial parameter, and a larger G-virial is related to a larger chance of being gravitationally bound. Therefore, the method provides a global picture of gravity in the PPV space. Using a hydrodynamical simulation model and a simple spherical-symmetric model, we demonstrate the connection between G-virial calculated in the observed PPV data cube and the G-virial calculated from the model. We found that the two are positively related. A larger G-virial is therefore linked to a larger chance of being gravitationally bound. Different from the virial parameter which quantifies self-gravity, the G-virial quantifies the effect of global gravity on the gas where all the interactions between all the particles in the 3D data cubes have been taken into account.

A map of this kind enables us to identify regions in molecular clouds in terms of gravitationally coherent regions. Compared with previous ways of defining regions based on emission, the regions identified from the G-virial maps more coherent and are less dependent on the technical parameters. Another advantage of such a definition is that the regions identified are coherent under gravity and are likely to collapse on their own.

We also demonstrated how to use the G-virial maps to quantify the structures of the identified gas condensations in terms of mass-radius and velocity dispersion-radius relations. We found that both the mass-radius relation and the velocity-dispersion relation of the model can be reconstructed with the help of the G-virial with a good fidelity when the model is symmetric. If the model is not symmetric, the G-virial map can be used to quantify the structures of the gas condensations, and it allows us to compare different structures.

As examples, we analyzed the  $^{13}\text{CO}(1-0)$  emission from the Perseus and Ophiuchus molecular clouds, and found that both can be decomposed into several regions which are gravitationally coherent (Fig. 8). Moreover, the cluster-bearing regions show higher values of G-virial at the centers which implies that gravity plays a more prominent role in these parts (Fig. 11). We carried out an analysis of a total of five regions identified in the Perseus and Ophiuchus molecular cloud, and derived mass-size relations and velocity dispersion-size relations for the regions. We also found that cluster-bearing regions are more massive at a given radius than those which do not bear a cluster (Fig. 12), and the cluster-bearing regions have a higher velocity dispersion at the outer parts (Fig. 13).

The method is general and can be applied to a variety of objects observed in 3D PPV space where gravity is supposed to play a role, and from the observations the method offers ways to quantify and compare these structures. We leave these possibilities for further explorations.

The importance of gravity in molecular clouds remains unclear. The effect of gravity as compared to kinetic motion is usually quantified using the virial parameter. The major uncertainty of the virial parameter comes from the definition of boundaries of the regions. With the G-virial method, we can eliminate this uncertainty by focusing on the regions that are gravitationally coherent. As shown in Fig. 14, the G-virial-defined regions are much closer to being gravitationally bound than the giant molecular clouds studied in Heyer et al. (2009). A study of a larger sample of molecular clouds can potentially tell if gravity is important throughout the Milky Way molecular clouds, and we leave this for a further study.

## 7.2. Caveats

Like all the other methods that quantify the ISM structures, our method is influenced by the line-of-sight confusion. One advantage of our method is that the line-of-sight confusion can be reduced by taking the velocity information into account. For a single object, if the velocity dispersion increases with radius, the G-virial method can take this into account and reduce the line-of-sight confusion effect. If different objects have different velocities, they will be separated easily. If different objects with comparable mass velocity are found on the same line of sight, the G-virial method becomes inaccurate.

The G-virial is a relative measure of the gravitational boundedness. As a result, it is not possible to tell whether a region is gravitationally bound based on the G-virial. However, a larger G-virial value means a region is more likely to be gravitationally bound. It is also possible to derive the virial parameter afterwards based on the iso-G-virial contours.

## Code Bibliography

astropy <http://www.astropy.org/>  
 astrodendro <https://dendrograms.readthedocs.org/en/latest/>  
 G-virial <http://gxli.github.io/G-virial/>  
 yt <http://yt-project.org/>

*Acknowledgements.* Guang-Xing Li is supported for this research through a stipend from the International Max Planck Research School (IMPRS) for Astronomy and Astrophysics at the Universities of Bonn and Cologne. Guang-Xing Li thanks Dr. Ke-Jia Lee for helping with the calculations and thanks Dr. Arnaud Belloche for discussions. We thank Eve Ostriker and Hao Gong for email exchanges. This study makes use of data from the COMPLETE survey. We also thank the yt and astrodendro teams for making their codes available, and would like to thank Thomas Robitaille for email exchanges. Dr. James Urquhart and Rosie Chen are acknowledged for careful readings of the draft and for their helpful comments. We thank the anonymous referee for several thorough and careful reviews of the paper and his/her insightful comments, and thank Malcolm Walmsley for his efforts.

## Appendix A: Relation between G-virial and the virial parameter

The relative importance between gravitational and kinetic energy is usually characterized with the virial parameter, which is introduced in Bertoldi & McKee (1992). To evaluate the virial parameter, it is necessary to define a structure on which the virial parameter is calculated.

One difference between G-virial and the virial parameter is that to evaluate the G-virial no such boundary is needed. Therefore the G-virial can be viewed as a generalization of the virial parameter to a continuous distribution of mass.

To illustrate the physical meaning of the G-virial, we define a quantity called particle virial, p-virial, which is the ratio between the gravitational energy of a particle to its kinetic energy  $\alpha_{p\text{-virial}} = E_p/2E_k$ . The potential energy  $E_p$  is determined by  $m \times \phi$  where  $m$  is the mass of the particle and  $\phi$  is the gravitation potential, and  $E_k$  is determined as  $1/2 \times m (v - v_c)^2$ . To define the kinetic energy, the velocity of the center of mass  $v_c$  is needed. Therefore p-virial is only suitable in the cases where a center of mass can be easily found. In the case of a molecular cloud, this is not straightforward because inside a molecular cloud the condensations can move at different velocities. The velocity of the center of mass depends on which clumps are included in the calculation, which is not unique. This difficulty is illustrated in Fig. A.1.



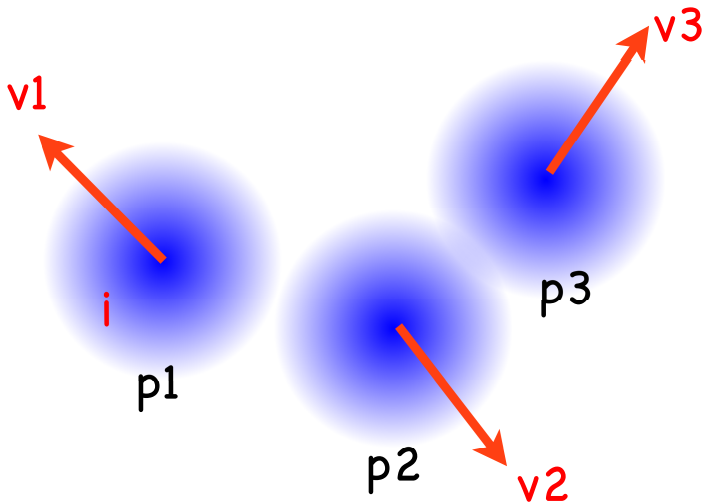


Fig. A.1: The difficulty of finding a proper center of mass. We consider three clumps p1, p2, p3 moving at velocities v1, v2, v3. If we are interested in whether *i* is gravitationally bound, since the majority of attraction comes from p1, physically the center of mass should be the center of mass of p1 instead of the center of mass of the three clumps p1, p2, p3, since p2 and p3 do not contribute much gravitational attraction to *i* compared to p1. Therefore to estimate the gravitational boundedness, a naive calculation of the center of mass where all the mass in the whole cloud is included is not appropriate. In the case of a complicated distribution of gas, finding the center of mass is not straightforward.

One major advantage of the G-virial over the *p-virial* is that no center of mass is needed. The G-virial is the sum of the gravitational boundedness, and to evaluate it we do not need to introduce the center of mass. Therefore, the G-virial can provide estimates of the importance of gravity when the geometry of the object is complicated and the center of mass is not well defined.

## Appendix B: Dependence on of G-virial the smoothing velocity $c_0$

The only free parameter in our method is the smoothing velocity  $c_0$  in Eq. 6. We added this parameter to avoid the divergence of Eq. 6 when the separation of velocity is zero.

Physically, if the velocity separation is zero, and if two gas particles spatially coincide with each other, the gravitational interaction will cause them to collide. However, the velocity separation cannot be zero since the gas also has velocity dispersions that have either thermal or non-thermal origin (Larson 1981). A physically lower limit of  $c_0$  should be the sound speed.

In reality, this is also affected by the superposition along the line of sight, since different gases that are physically unassociated can stay along the same line of sight and therefore appear to be gravitationally bound. Therefore, it is difficult to find a unique value of  $c_0$  based on first principles. In our case, we choose  $c_0$  to be 1 km/s, which is larger than and still comparable to the sound speed.

Here we investigate how our results can be affected by the parameter  $c_0$ . First, we made a G-virial map by assuming  $c_0 = 1$  km/s and then we made another map by assuming  $c_0 = 2$  km/s. Finally, we made a voxel-by-voxel comparison of the maps (Fig. B.1). We found the major effect of changing  $c_0$

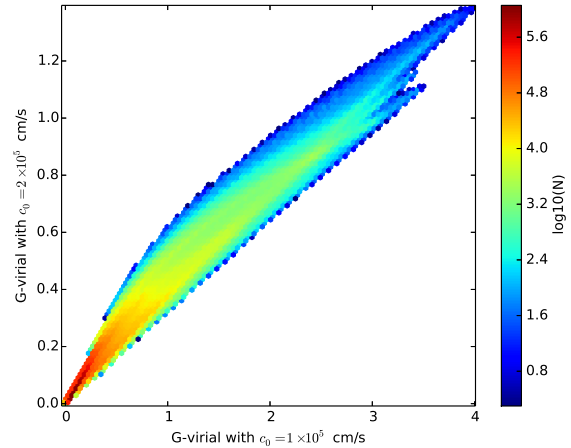


Fig. B.1: A comparison of G-virial map of the Ophiuchus molecular cloud under different  $c_0$ . The horizontal axis is the G-virial calculated assuming  $c_0 = 1$  km/s and the vertical axis is the G-virial calculated assuming  $c_0 = 2$  km/s. The grayscale image stands for the number of voxels that fall into each bin.

on the absolute values of G-virial: if we change  $c_0$  to 2 km/s the G-virial decreases by a factor of  $\sim 2$ . However, there is good correspondence between the old and new G-virial values. Therefore, changing  $c_0$  affects the absolute values of the G-virial; however, the relative values are unaffected. Therefore, all our figures should be unaffected by a change of  $c_0$  and the G-virial axes of Fig. 10 and Fig. 11 will change accordingly.

In the case where the G-virial is applied to different data cubes, in order for the results to be comparable, a unique choice of  $c_0$  is necessary.

## Appendix C: 3D renderings of G-virial of the Perseus and Ophiuchus molecular clouds

In order to provide intuitive representations of our G-virial maps, we present volume renderings of the 3D PPV data cubes with yt (Turk et al. 2011) in Fig. 7. **A movie can be found in <https://vimeo.com/115595991>.**

## Appendix D: Comparison with other methods

The previous methods to quantify the structure of molecular condensations such as Clumpfind and Dendrogram focus on the structure traced by the intensity map. The Clumpfind method tends to produce isolated structures. The Dendrogram produces hierarchical representations of the nested isosurfaces in 3D molecular line data cubes, and offers multi-scale decompositions. It can be applied to a much larger variety of situations. Both methods work in 2D (position-position) and 3D (PPV) space and both methods decompose the data to some extent.

The G-virial method presented in this paper is also based on a map of intensity in 3D PPV space. However, its output is neither a list of structures (as in the case of the Clumpfind) nor a tree representation of a hierarchy of structures (as in the gas of the Dendrogram). Instead, it produces a map of the importance of gravity in the 3D PPV. The output is also a map 3D PPV space. The G-virial map itself does not provide a decomposition of

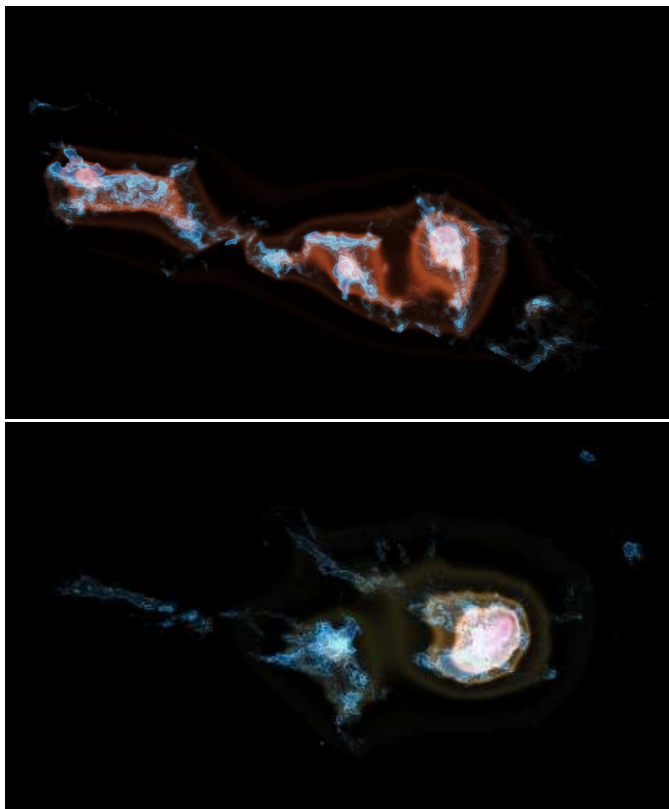


Fig. C.1: Volume rendering representations of the  $^{13}\text{CO}(1-0)$  emission and the corresponding G-virial map. The upper panel shows the result from the Perseus molecular cloud and the lower panel shows the result from the Ophiuchus molecular cloud. Blue stands for  $^{13}\text{CO}(1-0)$  emission and red and orange stand for G-virial. Both clouds are projected along the velocity direction. For the Perseus molecular cloud, the iso-surfaces of  $^{13}\text{CO}(1-0)$  emission start from 0.3 K and increase in steps of 0.64 K. The contours of the G-virial starts from 1.2 and increase in steps of 0.8. For the Ophiuchus molecular cloud, the contours of  $^{13}\text{CO}(1-0)$  emission start from 0.3 K and increase in steps of 1.24 K. The contours of the G-virial starts from 1.2 and increase in steps of 0.8.

the data. To decompose the cloud into regions and to analyze their properties, other methods are needed.

In this work, we use the Dendrogram to identify gravitationally coherent regions from the G-virial map, and use the iso-G-virial contours to quantify the properties of the regions in the  $M-r$  and  $\sigma_v-r$  plane. The G-virial method is not a replacement of the other methods, but it provides a new map on which those methods could be applied.

## References

- André, P., Belloche, A., Motte, F., & Peretto, N. 2007, *A&A*, 472, 519  
 Ballesteros-Paredes, J. 2006, *MNRAS*, 372, 443  
 Beaumont, C. N., Offner, S. S. R., Shetty, R., Glover, S. C. O., & Goodman, A. A. 2013, *ApJ*, 777, 173  
 Bertoldi, F. & McKee, C. F. 1992, *ApJ*, 395, 140  
 Blake, G. A., Sutton, E. C., Masson, C. R., & Phillips, T. G. 1987, *ApJ*, 315, 621  
 de Geus, E. J., de Zeeuw, P. T., & Lub, J. 1989, *A&A*, 216, 44  
 Dib, S., Bell, E., & Burkert, A. 2006, *ApJ*, 638, 797  
 Enoch, M. L., Young, K. E., Glenn, J., et al. 2006, *ApJ*, 638, 293  
 Federrath, C., Klessen, R. S., & Schmidt, W. 2008, *ApJ*, 688, L79  
 Federrath, C., Roman-Duval, J., Klessen, R. S., Schmidt, W., & Mac Low, M.-M. 2010, *A&A*, 512, A81

- Goldsmith, P. F., Heyer, M., Narayanan, G., et al. 2008, *ApJ*, 680, 428  
 Gong, H. & Ostriker, E. C. 2011, *ApJ*, 729, 120  
 Goodman, A. A., Rosolowsky, E. W., Borkin, M. A., et al. 2009, *Nature*, 457, 63  
 Gutermuth, R. A., Megeath, S. T., Myers, P. C., et al. 2009, *ApJS*, 184, 18  
 Heyer, M., Krawczyk, C., Duval, J., & Jackson, J. M. 2009, *ApJ*, 699, 1092  
 Heyer, M. H. & Brunt, C. M. 2004, *ApJ*, 615, L45  
 Kauffmann, J., Pillai, T., & Goldsmith, P. F. 2013, *ArXiv e-prints*  
 Kauffmann, J., Pillai, T., Shetty, R., Myers, P. C., & Goodman, A. A. 2010a, *ApJ*, 712, 1137  
 Kauffmann, J., Pillai, T., Shetty, R., Myers, P. C., & Goodman, A. A. 2010b, *ApJ*, 716, 433  
 Kirk, H., Pineda, J. E., Johnstone, D., & Goodman, A. 2010, *ApJ*, 723, 457  
 Langer, W. D. & Penzias, A. A. 1990, *ApJ*, 357, 477  
 Larson, R. B. 1981, *MNRAS*, 194, 809  
 Lazarian, A. & Pogosyan, D. 2004, *ApJ*, 616, 943  
 McKee, C. F. & Tan, J. C. 2003, *ApJ*, 585, 850  
 Men'shchikov, A., André, P., Didelon, P., et al. 2010, *A&A*, 518, L103  
 Pichardo, B., Vázquez-Semadeni, E., Gazol, A., Passot, T., & Ballesteros-Paredes, J. 2000, *ApJ*, 532, 353  
 Ridge, N. A., Di Francesco, J., Kirk, H., et al. 2006, *AJ*, 131, 2921  
 Roman-Duval, J., Federrath, C., Brunt, C., et al. 2011, *ApJ*, 740, 120  
 Roman-Duval, J., Jackson, J. M., Heyer, M., Rathborne, J., & Simon, R. 2010, *ApJ*, 723, 492  
 Rosolowsky, E. W., Pineda, J. E., Kauffmann, J., & Goodman, A. A. 2008, *ApJ*, 679, 1338  
 Schneider, S. & Elmegreen, B. G. 1979, *ApJS*, 41, 87  
 Shetty, R., Collins, D. C., Kauffmann, J., et al. 2010, *ApJ*, 712, 1049  
 Simon, R., Jackson, J. M., Clemens, D. P., Bania, T. M., & Heyer, M. H. 2001, *ApJ*, 551, 747  
 Smith, R. J., Clark, P. C., & Bonnell, I. A. 2009, *MNRAS*, 396, 830  
 Turk, M. J., Smith, B. D., Oishi, J. S., et al. 2011, *ApJS*, 192, 9  
 Walsh, A. J., Myers, P. C., & Burton, M. G. 2004, *ApJ*, 614, 194  
 Whiting, M. T. 2012, *MNRAS*, 421, 3242  
 Williams, J. P., Blitz, L., & McKee, C. F. 2000, *Protostars and Planets IV*, 97  
 Williams, J. P., de Geus, E. J., & Blitz, L. 1994, *ApJ*, 428, 693